INTERNATIONAL JOURNAL FOR NUMERICAL METHODS IN ENGINEERING
Int. J. Numer. Meth. Engng 2003; **58**:2041–2064 (DOI: 10.1002/nme.946)

An enriched finite element method and level sets for axisymmetric two-phase flow with surface tension

Jack Chessa[1] and Ted Belytschko[2,*,†]

[1] *Mechanical and Industrial Engineering Department, University of Texas at El Paso, El Paso, TX 79968, U.S.A.*
[2] *Department of Mechanical Engineering, Northwestern University, 2145 Sheridan Road, Evanston, IL 60208, U.S.A.*

SUMMARY

A finite element method for axisymmetric two-phase flow problems is presented. The method uses an enriched finite element formulation, in which the interface can move arbitrarily through the mesh without remeshing. The enrichment is implemented by the extended finite element method (X-FEM) which models the discontinuity in the velocity gradient at the interface by a local partition of unity. It provides an accurate representation of the velocity field at interfaces on an Eulerian grid that is not conformal to the weak discontinuity. The interface is represented by a level set which is also used in the construction of the element enrichment. Surface tension effects are considered and the interface curvature is computed from the level set field. The method is demonstrated by several examples. Copyright © 2003 John Wiley & Sons, Ltd.

KEY WORDS: enriched finite element; X-FEM; level sets; two-phase flow

1. INTRODUCTION

Dynamic axisymmetric flows encompass a wide array of flows including drops, jets, plumes, thin films and bubbles. These systems exhibit such diverse phenomena as capillary instabilities, Homman flow, fluid bridges, particulate and bubble flows, etc. In this paper, we consider incompressible flows of a primary fluid immersed in a secondary fluid. The interface between the two phases is either treated as a free boundary or as an interface in a multiphase flow. We approach this problem as a two-phase flow so we model the fluid in both phases by a single model with the interface defined by a level set. This approach can also be used

*Correspondence to: Ted Belytschko, Department of Mechanical Engineering, Northwestern University, 2145 Sheridan Road, Evanston, IL 60208, U.S.A.
† E-mail: tedbelytschko@northwestern.edu

Contract/grant sponsor: Office of Naval Research

Received 21 April 2003
Revised 13 June 2003
Accepted 10 July 2003

Copyright © 2003 John Wiley & Sons, Ltd.

for single-phase free surface flows. We will consider surface tension effects since in these problems surface tension is often significant.

We assume a no-slip condition at the interface between the two phases. But owing to the discontinuity in the fluid viscosities, the velocity gradient will generally be discontinuous at the phase interface, which is often called a weak discontinuity. For standard finite element methods to capture the flow accurately the mesh must conform to the phase interface, and as the interface evolves the mesh must be updated as with Arbitrary Lagrangian Eulerian (ALE) methods. For purely Eulerian grids the fluid parameters are typically '*smoothed out*' in elements that are intersected by the phase interface. In contrast, the proposed method uses a velocity approximation that is enriched so that the discontinuity in the velocity gradient can be captured within elements [1]. This allows for a purely Eulerian grid to be used while maintaining a *sharp* representation of the phase interface. So, in a sense we have maintained the '*resolution*' of moving mesh schemes such as ALE methods but on a fixed grid.

The eXtended Finite Element Method (X-FEM) is employed to enrich the velocity approximation. This method was originally developed to solve fracture mechanics problems [2, 3] and has recently been applied to a wide variety of problems with discontinuities, singularities and localized regions of high gradients (i.e. boundary layers) [1, 4–8]. X-FEM utilizes the partition of unity property, proposed in Reference [9], of the finite element shape functions to incorporate arbitrary enrichment functions into the approximation.

As noted in Sukumar *et al.* [5], local partition of unity enrichments for discontinuous gradients present some difficulties not found in discontinuous approximations. Therefore, the velocity enrichment should be modified so that the blending elements, i.e. the elements between the enriched elements and the standard finite elements, meet the conditions presented in Chessa *et al.* [10] to ensure optimal convergence. In this paper, we treat the blending elements by a velocity enrichment that is modified so that the gradient of the velocity enrichment is minimized. This approach is similar to that taken by Sukumar *et al.* [5] for elastic problems.

To represent the phase interface we adopt a level set approach [11, 12]. This method has several advantages: by projecting the interface topology, which is of reduced dimension, to a field of the same dimension as the computational domain, the level set function can be directly used to construct the enrichment approximation. Also, the interface curvature needed for evaluation of the surface tension forces can readily be computed from the level set.

The outline of the paper is as follows: in Section 2, the governing equations for incompressible axisymmetric two-phase flow are summarized. Section 3 presents the enriched velocity approximation and the construction of the modified enrichment function. In Section 4, the level set/interface update procedure is discussed. In Sections 5 and 6, the discrete enriched finite element equations are given and in Section 7, the computation of the curvature and surface tension force is discussed. The computational procedure is summarized in Section 8. The method is then illustrated by some examples in Section 9 and conclusions are presented in Section 10.

2. GOVERNING EQUATIONS

A schematic of our problem is shown in Figure 1. The domain Ω is partitioned into Ω_1 and Ω_2 which are functions of time and correspond to fluids 1 and 2, respectively; Γ_{int} is the interface between the two fluids. We assume that both phases are homogeneous and incompressible,

Copyright © 2003 John Wiley & Sons, Ltd.

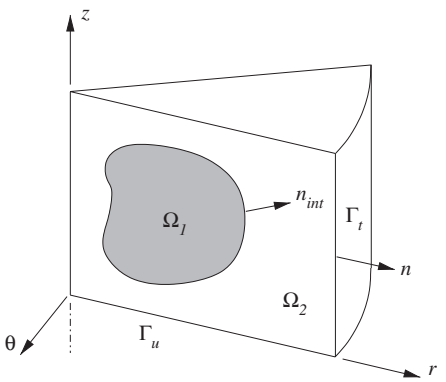


Figure 1. Problem statement.

so the material properties are constant in Ω_1 and Ω_2. For convenience, we consider the fluid density, ρ and viscosity, μ to be functions of position (and time) so

$$\rho(\boldsymbol{x}) = \begin{cases} \rho_1 & \forall \boldsymbol{x} \in \Omega_1(t) \\ \rho_2 & \forall \boldsymbol{x} \in \Omega_2(t) \end{cases} \tag{1}$$

$$\mu(\boldsymbol{x}) = \begin{cases} \mu_1 & \forall \boldsymbol{x} \in \Omega_1(t) \\ \mu_2 & \forall \boldsymbol{x} \in \Omega_2(t) \end{cases} \tag{2}$$

To track the interface we employ a level set function ϕ which is defined as

$$\phi(\boldsymbol{x}) = \begin{cases} -d(\boldsymbol{x}) & \forall \boldsymbol{x} \in \Omega_1 \\ d(\boldsymbol{x}) & \forall \boldsymbol{x} \in \Omega_2 \end{cases} \tag{3}$$

where $d(\boldsymbol{x})$ is the distance function of the interface Γ_{int} defined by

$$d(\boldsymbol{x}) = \min_{\boldsymbol{y} \in \Gamma_{\text{int}}} \|\boldsymbol{x} - \boldsymbol{y}\| \tag{4}$$

The use of the level set simplifies the update of the interface position as well as the computation of the curvature of the interface.

The Navier–Stokes equations for two-phase incompressible flow in a gravitational field with surface tension are

$$\rho \frac{\partial \boldsymbol{u}}{\partial t} + \rho \boldsymbol{u} \cdot \overrightarrow{\nabla} \boldsymbol{u} + \overrightarrow{\nabla} p = \overrightarrow{\nabla} \cdot (2\mu \boldsymbol{D}) + \rho \boldsymbol{g} + \delta(\phi(\boldsymbol{x})) \boldsymbol{f}^{\sigma} \tag{5}$$

$$\overrightarrow{\nabla} \cdot \boldsymbol{u} = \boldsymbol{0} \tag{6}$$

Copyright © 2003 John Wiley & Sons, Ltd.

where $\boldsymbol{u}$ is the velocity field, p the hydrostatic pressure, $\boldsymbol{g}$ the acceleration due to gravity, $\boldsymbol{D}$ the rate of deformation tensor which is defined as

$$\boldsymbol{D} = \tfrac{1}{2}(\overrightarrow{\boldsymbol{\nabla}}\boldsymbol{u} + \boldsymbol{u}\overleftarrow{\boldsymbol{\nabla}}) \tag{7}$$

and $\boldsymbol{f}^{\sigma}$ is the surface tension. The surface tension is related to the interface curvature by

$$\boldsymbol{f}^{\sigma} = \sigma\kappa\boldsymbol{n}_{\text{int}} \tag{8}$$

where σ is the surface tension coefficient between the two phases, κ is the local curvature of the phase interface $\boldsymbol{n}_{\text{int}}$ is a normal to the interface, and $\delta()$ is the Dirac delta function that localizes the surface tension force to points on the interface.

Assuming axisymmetry, the Navier–Stokes equations in terms of the radial coordinate r and the azimuthal co-ordinate z are

$$\rho\left(\frac{\partial u_r}{\partial t} + u_r u_{r,r} + u_{r,z}\right) + p_{,r} = \mu\left\{\left[\frac{1}{r}(ru_r)_{,r}\right]_{,r} + u_{r,zz}\right\} + f_r^{\sigma}\delta(\phi) \tag{9}$$

$$\rho\left(\frac{\partial u_z}{\partial t} + u_r u_{z,r} + u_z u_{z,z}\right) + p_{,z} = \mu\left[\frac{1}{r}(ru_{z,r})_{,r} + u_{z,zz}\right] + \rho g_z + f_z^{\sigma}\delta(\phi) \tag{10}$$

where commas denote partial derivatives with the subsequent variable and subscripts denote the components of a vector field. The continuity equation is

$$u_{z,z} + \frac{1}{r}(ru_r)_{,r} = 0 \tag{11}$$

Although not necessary for axisymmetry, we assume that $u_\theta = 0$.

The boundary conditions for the problem are as follows: the velocity boundary condition

$$\boldsymbol{u}(\boldsymbol{x},t) = \bar{\boldsymbol{u}}(\boldsymbol{x},t) \quad \forall \boldsymbol{x} \in \Gamma_u \tag{12}$$

where $\bar{\boldsymbol{u}}$ is the prescribed velocity and the traction boundary condition

$$\boldsymbol{n}\cdot\boldsymbol{\sigma}(\boldsymbol{x},t) = \bar{\boldsymbol{T}}(\boldsymbol{x},t) \quad \forall \boldsymbol{x} \in \Gamma_t \tag{13}$$

where $\bar{\boldsymbol{T}}$ is the prescribed traction. The traction boundary condition can be decomposed into its hydrostatic (pressure) and deviatoric (shear stress) parts as follows:

$$p(\boldsymbol{x},t) = \bar{p}(\boldsymbol{x},t) \quad \forall \boldsymbol{x} \in \Gamma_t \tag{14}$$

$$\boldsymbol{n}\cdot\boldsymbol{\tau}(\boldsymbol{x},t) = \bar{\boldsymbol{t}}(\boldsymbol{x},t) \quad \forall \boldsymbol{x} \in \Gamma_t \tag{15}$$

where p is the pressure and $\boldsymbol{\tau}$ is the deviatoric stress.

3. ENRICHED FINITE ELEMENT APPROXIMATIONS

The domain of the problem, Ω is discretized into elements Ω_e with a set of nodes $\{\boldsymbol{x}_I\}$, $I = 1$ to nn. The interpolation function (shape function) associated with node I is denoted

Copyright © 2003 John Wiley & Sons, Ltd.

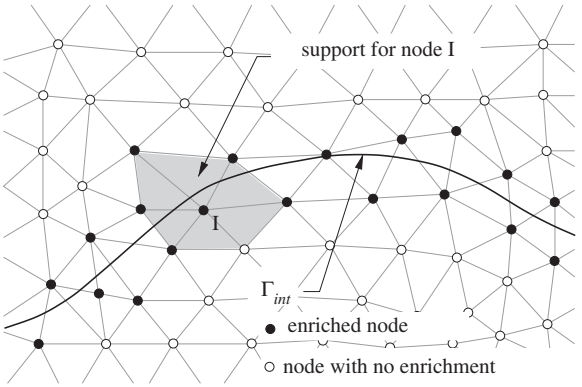


Figure 2. A typical finite element mesh with interface Γ_{int} showing the support of a generic node I and the enriched nodes.

by $N_I(\boldsymbol{x})$ and the set of all nodes by $\mathcal{N}$. The support of $N_I(\boldsymbol{x})$, which is the area over which it is non-zero, consists of the elements connected to the node I, so the support is compact. The support of a typical node I is shown in Figure 2. Since we are dealing with second-order partial differential equations (5), we choose the shape functions to be piecewise continuously differentiable, i.e. $C^0(\Omega)$.

The extended finite element approximation is constructed in terms of the level set function (3) and the shape functions N_I. The level set function is approximated by a standard finite element basis

$$\phi(\boldsymbol{x},t) = \sum_{I\in\mathcal{N}} N_I(\boldsymbol{x})\,\phi_I(t) \tag{16}$$

So the geometry of the interface is described by the nodal values of the level set function ϕ_I.

The extended finite element approximation constitutes a local partition of unity, as distinguished from the global partition of unity developed in References [9, 13]; see Reference [10]. In constructing the approximation we distinguish between the nodes whose support is intersected by the interface Γ_{int} and those nodes whose support is not intersected; the former set of nodes is called the set of enriched nodes and is denoted by $\mathcal{N}^{\text{enr}}$. Figure 2 illustrates the enriched nodes for a typical example. The enriched approximation is given by

$$\boldsymbol{u}^h(\boldsymbol{x},t) = \sum_{I\in\mathcal{N}} N_I(\boldsymbol{x})\boldsymbol{u}_I(t) + \sum_{J\in\mathcal{N}^{\text{enr}}} N_J(\boldsymbol{x})(|\phi^h(\boldsymbol{x},t)| - |\phi^h(\boldsymbol{x}_J,t)|)\boldsymbol{a}_J(t) \tag{17}$$

where $\boldsymbol{u}_I(t)$ are the nodal velocities for the standard finite element approximation and $\boldsymbol{a}_J(t)$ are additional nodal parameters at the enriched node J. The first term in (17) is simply the standard finite element approximation and the second term is the enriched part of the approximation. For convenience, we can express the enriched approximation as

$$\boldsymbol{u}^h(\boldsymbol{x},t) = \sum_{I\in\mathcal{N}} N_I(\boldsymbol{x})\boldsymbol{u}_I(t) + \sum_{J\in\mathcal{N}^{\text{enr}}} N_J^{\text{enr}}(\boldsymbol{x},t)\boldsymbol{a}_J(t) \tag{18}$$

Copyright © 2003 John Wiley & Sons, Ltd.

where

$$N_J^{\text{enr}}(\boldsymbol{x},t) = N_J(\boldsymbol{x})\Psi_J(\boldsymbol{x},t) \tag{19}$$

$$\Psi_J(\boldsymbol{x},t) = |\phi^h(\boldsymbol{x},t)| - |\phi^h(\boldsymbol{x}_J,t)| \tag{20}$$

The second term in the enrichment function Ψ_J in (20) is not essential but yields the desirable property that $\boldsymbol{u}^h(\boldsymbol{x}_I,t) = \boldsymbol{u}_I(t)$.

Next we examine the character of this approximation in the vicinity of the interface Γ_{int}. Taking the gradient of (17) we obtain

$$\overrightarrow{\boldsymbol{\nabla}}\boldsymbol{u}^h = \sum_{I\in\mathcal{N}} \overrightarrow{\boldsymbol{\nabla}}N_I \otimes \boldsymbol{u}_I(t) + \sum_{J\in\mathcal{N}^{\text{enr}}} (\overrightarrow{\boldsymbol{\nabla}}N_J\Psi_J + N_J\overrightarrow{\boldsymbol{\nabla}}\Psi_J) \otimes \boldsymbol{a}_J(t) \tag{21}$$

On the open set $\Omega\backslash\Gamma_{\text{int}}$

$$\overrightarrow{\boldsymbol{\nabla}}\Psi_J = \text{sign}(\phi)\overrightarrow{\boldsymbol{\nabla}}\phi = \text{sign}(\phi)\boldsymbol{n}_{\text{int}} \tag{22}$$

where sign$(\cdot)$ is the sign function and the second equality follows from the fact that ϕ is defined as a distance function and therefore $\boldsymbol{n}_{\text{int}} = \overrightarrow{\boldsymbol{\nabla}}\phi$, see (3)–(4). Substituting (22) into (21) provides

$$\overrightarrow{\boldsymbol{\nabla}}\boldsymbol{u}^h = \sum_{I\in\mathcal{N}} \overrightarrow{\boldsymbol{\nabla}}N_I \otimes \boldsymbol{u}_I(t) + \sum_{J\in\mathcal{N}^{\text{enr}}} (\overrightarrow{\boldsymbol{\nabla}}N_J\Psi_J + N_J\,\text{sign}(\phi)\boldsymbol{n}_{\text{int}}) \otimes \boldsymbol{a}_J(t) \tag{23}$$

Therefore, the jump in velocity $\boldsymbol{u}^h(\boldsymbol{x},t)$ across the interface is given by

$$[\![\overrightarrow{\boldsymbol{\nabla}}\boldsymbol{u}^h]\!] = 2\sum_{J\in\mathcal{N}^{\text{enr}}} N_J(\boldsymbol{x})\boldsymbol{n}_{\text{int}}(\boldsymbol{x},t) \otimes \boldsymbol{a}_J \quad \forall\boldsymbol{x}\in\Gamma_{\text{int}} \tag{24}$$

and

$$[\![\boldsymbol{n}_{\text{int}} \cdot \overrightarrow{\boldsymbol{\nabla}}\boldsymbol{u}^h(\boldsymbol{x},t)]\!] = 2\sum_{J\in\mathcal{N}^{\text{enr}}} N_J(\boldsymbol{x})\boldsymbol{a}_J \quad \forall\boldsymbol{x}\in\Gamma_{\text{int}} \tag{25}$$

The magnitude of the jump depends on $\boldsymbol{a}_I(t)$ and is C^0 along the interface as can be seen from (25). Note, that as with all piecewise continuous finite element approximations, $[\![\overrightarrow{\boldsymbol{\nabla}}\boldsymbol{u}^h]\!] \neq 0$ on the element edges, see Reference [14].

The enrichment functions and shape functions for a linear two-node element in one dimension are shown in Figure 3. Each enrichment function is a product of the shape function N_I and the corresponding enrichment function $\Psi(\boldsymbol{x},t)$. The enriched shape functions vanish at the nodes. The enriched shape functions for a three-node linear right isosceles triangle with a discontinuous derivative parallel to one leg are shown in Figure 4. As can be seen, each enrichment function vanishes along two of the edges. On the third edge a kink, similar to what appears in the one-dimensional element, can be seen.

The enrichment is of two types. In elements cut by the interface; all nodes are enriched and the enrichment is a partition of unity [13], so the enrichment function $\Psi(\boldsymbol{x},t)$ is reproduced exactly. On the other hand, in elements adjacent to the fully enriched elements, not all of the nodes are enriched and therefore the enrichment is not a partition of unity. In these *partially* enriched elements the enrichment *blends* the enrichment so that it vanishes at the edge of

Copyright © 2003 John Wiley & Sons, Ltd.

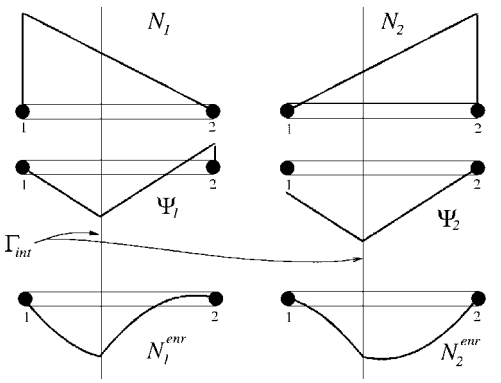


Figure 3. Example of an enriched finite element shape functions in $\mathbb{R}^1$.

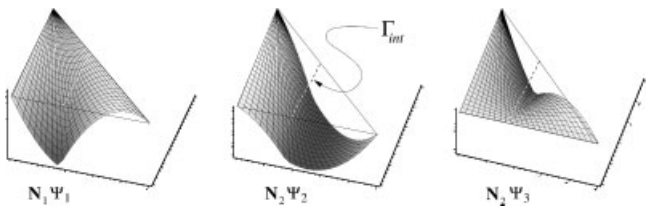


Figure 4. Enriched finite element shape functions for a three-node linear triangular element.

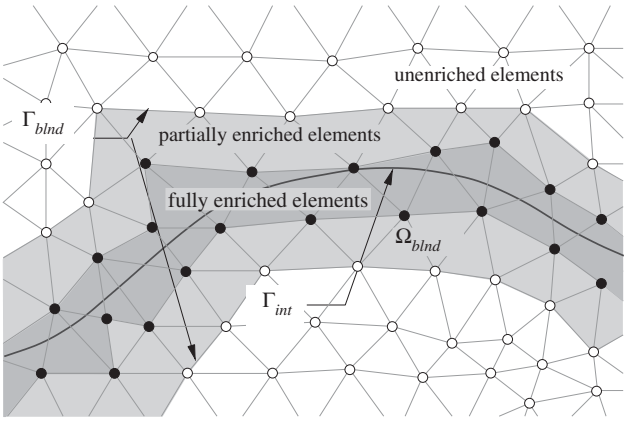


Figure 5. Local partition of unity enrichment for a typical finite element mesh with an interface, showing elements that are fully enriched, partially enriched and unenriched. Also shown is the boundary Γ_{blnd} where the enrichment vanishes.

the support. These domains of fully enriched and partially enriched elements are illustrated in Figure 5. The enrichment functions have compact support so the resulting system matrices are sparse.

Copyright © 2003 John Wiley & Sons, Ltd.

The enrichment, since it is a local partition of unity [10], modifies the velocity field only in the elements crossed by the interface and in the adjacent elements, see Figure 5. In other words, only the elements that lie entirely within the supports of shape functions cut by the interface are affected by the enrichment. The additional degrees of freedom $\boldsymbol{a}_J$ can be treated either by adding nodes to the element or increasing the number of degrees of freedom for the enriched nodes. In either case, the modifications required in a standard finite element code are modest.

3.1. Velocity enrichment modification

As discussed by Chessa *et al.* [10], local partition of unity enrichment schemes for discontinuous gradients (17) require care in the construction of the blending elements. Incorrect construction of the blending elements may reduce convergence and accuracy. Conditions to ensure optimal convergence as well as some examples of correctly constructed blending elements are presented in Reference [10].

One approach for improving the performance of local partition of unity enrichments is to construct the enrichment function $\Psi(\boldsymbol{x})$ so that the gradient is minimized in the blending elements; this is the approach taken by Sukumar *et al.* [5]. This is accomplished by constructing the velocity enrichment in terms of a modified level set function $\hat{\phi}(\boldsymbol{x},t)$

$$\boldsymbol{u}^h(\boldsymbol{x},t)=\sum_{I\in\mathcal{N}} N_I(\boldsymbol{x})\boldsymbol{u}_I(t)+\sum_{J\in\mathcal{N}^{\mathrm{enr}}} N_J(\boldsymbol{x})(|\hat{\phi}^h(\boldsymbol{x},t)|-|\hat{\phi}(\boldsymbol{x}_J,t)|)\boldsymbol{a}_J(t) \tag{26}$$

The modified level set functions is constructed so that $\vec{\nabla}\hat{\phi}$ is minimized in the blending elements. The modified level set function $\hat{\phi}$ is defined by the finite element basis

$$\hat{\phi}(\boldsymbol{x},t)=\sum_{I\in\mathcal{N}} N_I(\boldsymbol{x})\hat{\phi}_I(t) \tag{27}$$

It is constructed by minimizing the following functional on Ω^{blnd}

$$I(\hat{\phi})\equiv\frac{1}{2}\int_{\Omega^{\mathrm{blnd}}}\vec{\nabla}\hat{\phi}\cdot\vec{\nabla}\hat{\phi}\,\mathrm{d}\Omega \tag{28}$$

with the essential boundary condition

$$\hat{\phi}(\boldsymbol{x})=\phi(\boldsymbol{x})\quad\forall\boldsymbol{x}\in\Gamma^{\mathrm{blnd}} \tag{29}$$

where Γ^{blnd} is shown in Figure 5.

The minimization yields the following discrete equations for $\hat{\boldsymbol{\Phi}}=\{\hat{\Phi}_J(t^n)\}_{J\in\mathcal{N}}$ at a given time t^n

$$\mathbf{K}^{\hat{\phi}}\hat{\boldsymbol{\Phi}}^n=\mathbf{0} \tag{30}$$

where

$$\mathbf{K}^{\hat{\phi}}=\int_{\Omega^{\mathrm{blnd}}}(\vec{\nabla}\mathbf{N})^{\mathrm{T}}\vec{\nabla}\mathbf{N}\,\mathrm{d}\Omega \tag{31}$$

Copyright © 2003 John Wiley & Sons, Ltd.

Since (30) is only solved in the blended elements the expense of this operation is minimal. The effectiveness of this modified enrichment function will be illustrated in the first example problem in Section 9.1.

4. LEVEL SET FORMULATION

The level set function that tracks the interface is approximated by the same discretization that is used for the velocity and pressure fields (27).

In the update of a level set, its total derivative on the zero level set must vanish, so Equation (3) is updated by

$$\frac{\partial \phi}{\partial t} + \boldsymbol{u} \cdot \overrightarrow{\boldsymbol{\nabla}} \phi = 0 \tag{32}$$

The update method used here has been described in Reference [1].

5. NAVIER–STOKES FORMULATION

We solve the Navier–Stokes equations by a characteristic-based split (CBS) algorithm based on the projection method of Chorin [15] as described in References [16, 17]. In this method, an auxiliary velocity field $\boldsymbol{u}^*$ is introduced to uncouple the momentum and continuity equations; a characteristic method is used to stabilize the non-self-adjoint operators in (5). The CBS formulation of (5) can be written as

$$\rho^n \boldsymbol{u}^* = \rho^n \boldsymbol{u}^n - \Delta t \left[\rho \boldsymbol{u} \cdot \overrightarrow{\boldsymbol{\nabla}} \boldsymbol{u} - \overrightarrow{\boldsymbol{\nabla}} \cdot \boldsymbol{\tau} - \rho \boldsymbol{g} - \boldsymbol{f}^\sigma - \frac{\Delta t}{2} (\boldsymbol{u} \cdot \overrightarrow{\boldsymbol{\nabla}}) \left(\rho \boldsymbol{u} \cdot \overrightarrow{\boldsymbol{\nabla}} \boldsymbol{u} - \rho \boldsymbol{g} - \boldsymbol{f}^\sigma \right) \right] \Bigg|_{t=t^n} \tag{33}$$

where $\boldsymbol{\tau}$ is the shear stress which is defined as

$$\boldsymbol{\tau} = 2\mu \boldsymbol{D} \tag{34}$$

In each step, the velocity field is '*corrected*' by the pressure increment so that is divergence free

$$\rho^n \boldsymbol{u}^{n+1} = \rho^n \boldsymbol{u}^* - \Delta t \overrightarrow{\boldsymbol{\nabla}} p^{n+1} + \frac{\Delta t^2}{2} \left(\boldsymbol{u}^n \cdot \overrightarrow{\boldsymbol{\nabla}} \right) \overrightarrow{\boldsymbol{\nabla}} p^n \tag{35}$$

where $\boldsymbol{u}^*$ is the auxiliary velocity. Dividing by the density and taking the divergence of (35) (recall that the velocity at time t^{n+1} must be divergence free (6), we arrive at the following Poisson equation for the pressure:

$$\Delta t \overrightarrow{\boldsymbol{\nabla}} \cdot \left(\frac{1}{\rho^n} \overrightarrow{\boldsymbol{\nabla}} p^{n+1} \right) = \overrightarrow{\boldsymbol{\nabla}} \cdot (\boldsymbol{u}^*) \tag{36}$$

The Galerkin weak forms are given in Reference [1].

Copyright © 2003 John Wiley & Sons, Ltd.

6. ENRICHED FINITE ELEMENT EQUATIONS

Three node triangular element with linear velocity and linear pressure were used. The enriched finite element approximations for the enriched velocity test function $\boldsymbol{w}$ and trial function $\boldsymbol{u}$ are defined as follows:

$$\boldsymbol{w} = \bar{\mathbf{W}}^{\mathrm{T}} \bar{\mathbf{N}}^{n+1} \tag{37}$$

$$\boldsymbol{u}^n = (\bar{\mathbf{N}}^n)^{\mathrm{T}}\, \bar{\mathbf{U}}^n \tag{38}$$

$$\boldsymbol{u}^* = (\bar{\mathbf{N}}^{n+1})^{\mathrm{T}}\, \bar{\mathbf{U}}^* \tag{39}$$

with

$$\mathbf{N} = [N_1,\ N_2,\ \ldots\ N_{\mathrm{nn}}]^{\mathrm{T}} \tag{40}$$

$$\bar{\mathbf{N}}^n = \left[\begin{array}{cc} \mathbf{N} & \mathbf{0} \\ \mathbf{0} & \mathbf{N} \\ \mathbf{N}^{\mathrm{enr}} & \mathbf{0} \\ \mathbf{0} & \mathbf{N}^{\mathrm{enr}} \end{array}\right]\Bigg|_{t=t^n} \tag{41}$$

$$\bar{\mathbf{W}} = \begin{bmatrix} \mathbf{W} \\ \mathbf{V} \end{bmatrix} \tag{42}$$

$$\mathbf{W} = \left[w_{r1},\ w_{r1},\ \ldots,\ w_{r\,\mathrm{nn}},\ w_{z1},\ w_{z1},\ \ldots,\ w_{z\,\mathrm{nn}}\right]^{\mathrm{T}} \tag{43}$$

$$\mathbf{V} = [v_{r1},\ v_{r1},\ \ldots,\ v_{r\,\mathrm{nn}},\ v_{z1},\ v_{z1},\ \ldots,\ v_{z\,\mathrm{nn}}]^{\mathrm{T}} \tag{44}$$

$$\bar{\mathbf{U}}^n = \begin{bmatrix} \mathbf{U}^n \\ \mathbf{A}^n \end{bmatrix} \tag{45}$$

$$\mathbf{U}^n = [u^n_{r1},\ u^n_{r1},\ \ldots,\ u^n_{r\,\mathrm{nn}},\ u^n_{z1},\ u^n_{z1},\ \ldots,\ u^n_{z\,\mathrm{nn}}]^{\mathrm{T}} \tag{46}$$

$$\mathbf{A}^n = [a^n_{r1},\ a^n_{r1},\ \ldots,\ a^n_{r\,\mathrm{nn}},\ a^n_{z1},\ a^n_{z1},\ \ldots,\ a^n_{z\,\mathrm{nn}}]^{\mathrm{T}} \tag{47}$$

$$\bar{\mathbf{U}}^* = \begin{bmatrix} \mathbf{U}^* \\ \mathbf{A}^* \end{bmatrix} \tag{48}$$

$$\mathbf{U}^* = [u^*_{r1},\ u^*_{r1},\ \ldots,\ u^*_{r\,\mathrm{nn}},\ u^*_{z1},\ u^*_{z1},\ \ldots\ u^*_{z\,\mathrm{nn}}]^{\mathrm{T}} \tag{49}$$

$$\mathbf{A}^* = [a^*_{r1},\ a^*_{r1},\ \ldots,\ a^*_{r\,\mathrm{nn}},\ a^*_{z1},\ a^*_{z1},\ \ldots,\ a^*_{z\,\mathrm{nn}}]^{\mathrm{T}} \tag{50}$$

Copyright © 2003 John Wiley & Sons, Ltd.

The superscript n on $\bar{\mathbf{N}}^n$ indicates that the enriched shape functions are a function of time and nn is the number of nodes and $\mathbf{N}^{\text{enr}}$ is as defined in (19). The pressure test and trial functions are given by standard finite element approximations as follows:

$$q = \mathbf{Q}^{\mathrm{T}}\mathbf{N} \tag{51}$$

$$p^n = \mathbf{N}^{\mathrm{T}}\mathbf{P}^n \tag{52}$$

where

$$\mathbf{N} = [N_1,\ N_2,\ \ldots,\ N_{\text{nn}}]^{\mathrm{T}} \tag{53}$$

$$\mathbf{P}^n = [p_1^n,\ p_2^n,\ \ldots,\ p_{\text{nn}}^n]^{\mathrm{T}} \tag{54}$$

$$\mathbf{Q} = [q_1,\ q_2,\ \ldots,\ q_{\text{nn}}]^{\mathrm{T}} \tag{55}$$

Substituting (38)–(55) into the Galerkin form of Equations (33)–(36) we obtain the following discretized enriched finite element equations:

$$\mathbf{M}\,\bar{\mathbf{U}}^* = \mathbf{M}^n\,\bar{\mathbf{U}}^n - \Delta t\mathbf{f}^* \tag{56}$$

$$\mathbf{K}^p\mathbf{P}^{n+1} = \frac{1}{\Delta t}(\mathbf{G}\,\bar{\mathbf{U}}^* - \mathbf{f}^{\text{in}}) \tag{57}$$

$$\bar{\mathbf{U}}^{n+1} = \bar{\mathbf{U}}^* - \Delta t\mathbf{M}^{-1}\left(\mathbf{G}^{\mathrm{T}}\mathbf{P}^{n+1} + \frac{\Delta t}{2}\mathbf{f}^p\right) \tag{58}$$

where

$$\mathbf{f}^* = \mathbf{f}^{\text{adv}} + \mathbf{f}^{\text{visc}} - \mathbf{f}^{\text{shear}} - \mathbf{f}^{\text{ext}} + \frac{\Delta t}{2}\mathbf{f}^{\text{stab}} - \mathbf{f}^{\sigma} \tag{59}$$

and

$$\mathbf{M} = \int_\Omega \bar{\mathbf{N}}^{n+1}\rho^n(\bar{\mathbf{N}}^{n+1})^{\mathrm{T}}\,\mathrm{d}\Omega \tag{60}$$

$$\mathbf{M}^n = \int_\Omega \bar{\mathbf{N}}^{n+1}\rho^n(\bar{\mathbf{N}}^{n})^{\mathrm{T}}\,\mathrm{d}\Omega \tag{61}$$

$$\mathbf{f}^{\text{adv}} = \int_\Omega \bar{\mathbf{N}}^{n+1}\rho^n\,\boldsymbol{u}^n\cdot\vec{\boldsymbol{\nabla}}\boldsymbol{u}^n\,\mathrm{d}\Omega \tag{62}$$

$$\mathbf{f}^{\text{visc}} = \int_\Omega (\,\bar{\mathbf{B}}^{n+1})^{\mathrm{T}}\mathbf{T}^n\,\mathrm{d}\Omega \tag{63}$$

$$\mathbf{f}^{\text{shear}} = \int_{\Gamma_t} \bar{\mathbf{N}}^{n+1}\bar{\boldsymbol{t}}^n\,\mathrm{d}\Gamma \tag{64}$$

Copyright © 2003 John Wiley & Sons, Ltd.

$$\mathbf{f}^{\text{ext}} = \int_{\Omega} \bar{\mathbf{N}}^{n+1} \rho^n \boldsymbol{g} \, \mathrm{d}\Omega \tag{65}$$

$$\mathbf{f}^{\sigma} = \int_{\Omega} \bar{\mathbf{N}}^{n+1} \delta(\phi(\boldsymbol{x})) \kappa \sigma \boldsymbol{n}_{\text{int}} \, \mathrm{d}\Omega \tag{66}$$

$$\mathbf{f}^{\text{stab}} = \int_{\Omega} (\boldsymbol{u}^n \cdot \overrightarrow{\boldsymbol{\nabla}} \bar{\mathbf{N}}^{n+1})(\rho^n \boldsymbol{u}^n \cdot \overrightarrow{\boldsymbol{\nabla}} \boldsymbol{u}^n - \rho^n \boldsymbol{g} - \delta(\phi(\boldsymbol{x})) \boldsymbol{f}^{\sigma}) \, \mathrm{d}\Omega \tag{67}$$

$$\mathbf{K}^p = \int_{\Omega} \frac{1}{\rho^n} \overrightarrow{\boldsymbol{\nabla}} \mathbf{N} (\overrightarrow{\boldsymbol{\nabla}} \mathbf{N})^{\mathrm{T}} \, \mathrm{d}\Omega \tag{68}$$

$$\mathbf{f}^{\text{in}} = \int_{\Gamma_u} \mathbf{N} \boldsymbol{n} \cdot \bar{\boldsymbol{u}}^n \, \mathrm{d}\Gamma \tag{69}$$

$$\mathbf{G} = \int_{\Omega} \overrightarrow{\boldsymbol{\nabla}} \mathbf{N} (\bar{\mathbf{N}}^{n+1})^{\mathrm{T}} \, \mathrm{d}\Omega \tag{70}$$

$$\mathbf{f}^p = \int_{\Omega} (\boldsymbol{u}^n \cdot \overrightarrow{\boldsymbol{\nabla}} \bar{\mathbf{N}}^{n+1}) \overrightarrow{\boldsymbol{\nabla}} p^n \, \mathrm{d}\Omega \tag{71}$$

In the above $\mathbf{T}$ is the Voigt form of the deviatoric stress which is for a linear viscous law is given by

$$\mathbf{T}^n = (\mu \, \hat{\mathbf{I}}) \, \bar{\mathbf{B}}^n \, \bar{\mathbf{U}}^n \tag{72}$$

The matrix $\bar{\mathbf{B}}$, relates the rate of deformation tensor $\boldsymbol{D}$ to the nodal velocities and is given by

$$\bar{\mathbf{B}}^n = \begin{pmatrix} \dfrac{\partial}{\partial r} & 0 \\ 0 & \dfrac{\partial}{\partial z} \\ \dfrac{1}{r} & 0 \\ \dfrac{\partial}{\partial z} & \dfrac{\partial}{\partial r} \end{pmatrix} (\bar{\mathbf{N}}^n)^{\mathrm{T}} \tag{73}$$

and

$$\hat{\mathbf{I}} = \begin{bmatrix} 2 & & & \\ & 2 & & \\ & & 2 & \\ & & & 1 \end{bmatrix} \tag{74}$$

Copyright © 2003 John Wiley & Sons, Ltd.

When evaluating the gradient of the enriched shape functions $\bar{\mathbf{N}}$ the chain rule must be employed due to the spacial dependence of the level set field ϕ, so

$$\overrightarrow{\nabla}\bar{N}_I = \overrightarrow{\nabla}N_I\psi_I + N_I\overrightarrow{\nabla}\psi_I \tag{75}$$

In evaluating the element matrices and vectors for elements on the interface the quadrature rule must be able to treat discontinuous integrands. Quadrature rules for these enriched methods are described in References [3, 5, 7].

The standard (unenriched) degrees of freedom for the mass matrix $\mathbf{M}$ are lumped by a row sum method. For accuracy and stability reasons the enriched degrees of freedom cannot be lumped and as a result (56) and (58) should be solved by an implicit–explicit algorithm as in References [18, 19].

7. COMPUTATION OF INTERFACE CURVATURE AND SURFACE TENSION

The discretized surface tension force given by (66) involves a Dirac delta function. We replace the delta function δ by $\hat{\delta}(\eta)$, a regularized Dirac function, given by

$$\hat{\delta}(\eta) = \begin{cases} 0, & |\eta| > 1 \\ \frac{15}{16}(1 - 2\eta^2 + \eta^4), & |\eta| \leqslant 1 \end{cases} \tag{76}$$

with

$$\eta = \frac{\phi}{\varepsilon} \tag{77}$$

In the above equation ε is a parameter that controls the width of the support of the regularized delta function. Note that

$$\int_{\eta=-1}^{\eta=1} \hat{\delta}(\eta)\,\mathrm{d}\eta = 1 \tag{78}$$

Since the integrand is then a polynomial it can be numerically integrated with standard quadrature.

For axisymmetric domains the curvature κ in (66) is defined as

$$\kappa = \frac{1}{R_1} + \frac{1}{R_2} \tag{79}$$

where the principal radii of curvature are R_1 and R_2 as shown in Figure 6. Since the phase interface is represented by the hypersurface $\phi = 0$ (where ϕ is the level set function) the normal to the interface $\boldsymbol{n} = (n_r, n_z)$ is

$$\boldsymbol{n}_{\text{int}} = \frac{\overrightarrow{\nabla}\phi}{|\nabla\phi|} \tag{80}$$

Note that in the calculations, the right-hand side of (7) is normalized since the finite approximation of ϕ may deviate from the signed distance function. The in-plane curvature $\kappa_1 = 1/R_1$ is

$$\kappa_1 = \overrightarrow{\nabla} \cdot \boldsymbol{n}_{\text{int}} \tag{81}$$

Copyright © 2003 John Wiley & Sons, Ltd.

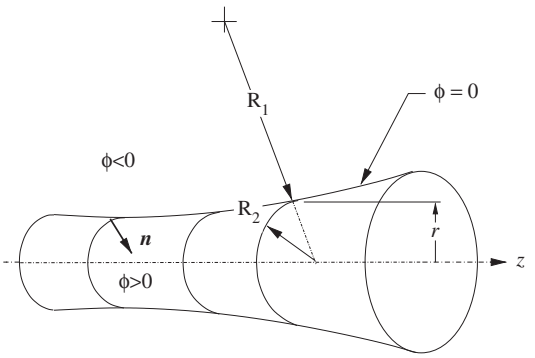


Figure 6. Radii of curvature used to compute surface tension in axisymmetric domains.

or in terms of the level set function

$$\kappa_1 = \vec{\nabla} \cdot \left(\frac{\vec{\nabla}\phi}{|\nabla\phi|} \right) \tag{82}$$

One difficulty in using (82) to directly compute the interface curvature is that for linear shape functions, approximations to $\nabla^2\phi$ vanish in element interiors. While it is possible to use higher-order elements in the level set approximation the implementation would be awkward. To circumvent this difficulty we calculate the following auxiliary fields about the interface to compute the curvature:

1. The gradient of the level set $\boldsymbol{g}$.
2. The in-plane curvature κ_1.

The fields are computed by minimizing the following functionals for $\boldsymbol{g}$ and κ_1, respectively,

$$I_g = \int_\Omega \frac{1}{2}(\boldsymbol{g} - \vec{\nabla}\phi)^2 \, \mathrm{d}\Omega \tag{83}$$

$$I_\kappa = \int_\Omega \frac{1}{2} \left[\kappa_1 - \vec{\nabla} \cdot \left(\frac{\boldsymbol{g}}{|g|} \right) \right]^2 \mathrm{d}\Omega \tag{84}$$

Using C^0 finite element approximations for $\boldsymbol{g}^h$ and κ_1^h, given by

$$\boldsymbol{g}^h = \sum_{I \in \mathcal{N}} N_I(\boldsymbol{x}) \boldsymbol{g}_I \tag{85}$$

$$\kappa_1^h = \sum_{I \in \mathcal{N}} N_I(\boldsymbol{x}) \kappa_{1I} \tag{86}$$

Copyright © 2003 John Wiley & Sons, Ltd.

in I_g and I_κ and minimizing with respect to the nodal unknowns $\boldsymbol{g}_I$ and κ_{1I} we arrive with the following discrete finite element equations for $\boldsymbol{g}_I$ and κ_{1I}:

$$\mathbf{M}^g\mathbf{g} = \mathbf{A}\phi \tag{87}$$

$$\mathbf{M}^\kappa\boldsymbol{\kappa} = \mathbf{f}(\boldsymbol{g}^h) \tag{88}$$

where

$$\mathbf{M}^g = \int_\Omega \mathbf{N}\mathbf{N}^{\mathrm{T}}\,\mathrm{d}\Omega\,\mathbf{I} \tag{89}$$

$$\mathbf{A} = \int_\Omega \mathbf{N}(\overrightarrow{\boldsymbol{\nabla}}\mathbf{N})^{\mathrm{T}}\,\mathrm{d}\Omega \tag{90}$$

$$\mathbf{M}^\kappa = \int_\Omega \mathbf{N}\mathbf{N}^{\mathrm{T}}\,\mathrm{d}\Omega \tag{91}$$

$$\mathbf{f} = \int_\Omega \mathbf{N}\overrightarrow{\boldsymbol{\nabla}}\cdot\left(\frac{\boldsymbol{g}^h}{|g^h|}\right)\mathrm{d}\Omega \tag{92}$$

and $\mathbf{I}$ is an identity matrix whose dimension equals the number of spacial dimensions (in the axisymmetric case two, r and z). These equations need only be solved on the elements near the interface, not on the entire computational domain. Another approach that may be simpler is to use a moving least-square approximation for the level set function, see References [20, 21].

The curvature, in the plane defined by R_1 and θ, κ_2 can be computed from geometrical considerations as follows:

$$\kappa_2 = \frac{n_r}{r} \tag{93}$$

where n_r is the radial component of the interface normal $\boldsymbol{n}_{\mathrm{int}}$ as shown in Figure 6.

8. UPDATE PROCEDURE

For each time step the update procedure for the proposed method is as follows:

0. Given $\boldsymbol{u}^n$, p^n and ϕ^n.
1. Compute ϕ^{n+1} from (32).
2. Compute $\boldsymbol{u}^*$ from (56).
3. Compute p^{n+1} from (57).
4. Compute $\boldsymbol{u}^{n+1}$ from (58).
5. $n \leftarrow n+1$; go to step 1.

Copyright © 2003 John Wiley & Sons, Ltd.

9. EXAMPLES

9.1. Fully developed Couette flow

Here we consider a fully developed Couette flow for two layered fluids through an axisymmetric channel. The two fluids are labeled as fluids 1 and 2, and they occupy Ω_1 and Ω_2, respectively. The interface between the two fluids is $r = r_i + h_1$ as shown in Figure 7. The purpose of this example is to illustrate the effect of the modified velocity enrichment function in capturing the discontinuity in the velocity gradient. Other features of the problem are as shown in Figure 7. The exact solution assuming fully developed flow is

$$u_z = \begin{cases} \alpha\mu_2(r - r_i), & r_i \leqslant r \leqslant r_i + h/2 \\ \alpha((\mu_2 - \mu_1)\frac{h}{2} + mu_1(r - r_i)), & r_i + h/2 < r < r_i + h \end{cases} \tag{94}$$

$$u_r = 0 \tag{95}$$

$$p = p_0 \tag{96}$$

where

$$\alpha = \frac{2U_0}{h(\mu_1 + \mu_2)} \tag{97}$$

If $L \gg h$ then the numerical problem is a good approximation to fully developed flow. The following parameters were used in this example: $L = 100$, $r_i = 5$, $h = 1$, $U_0 = 0.1$, $\rho_1 = \rho_2 = 1.0$, $\mu_1 = 1.0$ and $\mu_2 = 100$. Zero velocity and pressure initial conditions are used.

The velocity at the outer radius is linearly ramped up to U_0 over a time of 1.0. The problem is then run for another 10.0 time units at a step size of $\Delta t = 0.125$ to ensure that steady-state conditions are achieved.

The problem was run for three cases:

1. No velocity enrichment.
2. Velocity enrichment function $\Psi_u = |\phi|$.
3. Modified velocity enrichment function $\Psi_u = |\hat{\phi}|$.

Surface tension was ignored because it creates an instability in the phase interface. The velocity profile along $z = 0.75L$ is plotted in Figure 8 for the three cases, along with the velocity profile for the exact solution. Note that only the method with the modified velocity

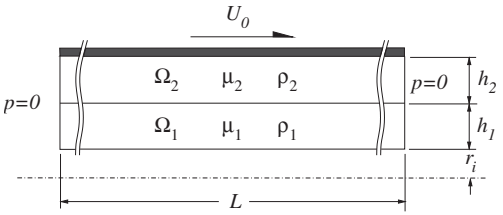


Figure 7. Axisymmetric Couette flow problem statement.

Copyright © 2003 John Wiley & Sons, Ltd.

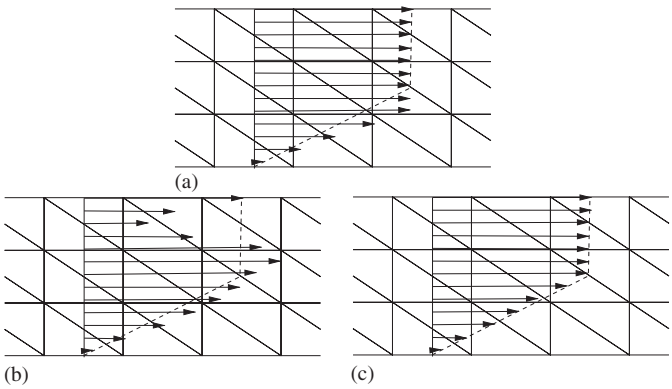


Figure 8. Velocity profiles for axisymmetric Couette flow at $z = 0.75L$. The numerical solutions are: (a) no velocity enrichment; (b) with old velocity enrichment; and (c) with the modified velocity enrichment. The numerical results denoted with the velocity vectors and the velocity profile for the exact solution (fully developed flow assumption) is denoted with the dashed line.

enrichment function provides the correct results. The case may be made that the enriched method without the modified enrichment function is no better than no enrichment at all.

9.2. Drop falling onto a thin film

We consider an initially spherical drop with surface tension falling under gravity to a thin film on a rigid support. The properties of the film and the drop are identical. The fluid and thin film are designated as fluid 1 and are surrounded by a second fluid designated as fluid 2. The initial configuration of the problem along with an unstructured mesh are shown in Figure 9.

The initial radius of the bubble $R = 0.25$, the initial height of the bubble above the film $h = 1.0$, the thickness of the film $t = 0.25$, the viscosity of fluid 1, $\mu_1 = 0.001$, the viscosity of fluid 2, $\mu_2 = 0.002$, the density of fluid 1, $\rho_1 = 2.0$, the density of fluid 2, $\rho_2 = 0.1$, the surface tension coefficient between the two fluids $\sigma = 1.0$ and the gravitational acceleration $g = 10.0$. The boundary conditions are as follows: zero pressure prescribed on the top edge, no slip on the bottom edge and zero shear traction on the right edge. The initial velocity and hydrostatic pressure were zero.

The computation was performed with the unstructured mesh shown in Figure 9 and a 25×46 structured mesh (each quadrilateral was subdivided into two triangles in the latter) to study the mesh dependence of the method. The results for the simulation are shown in Figures 10–12.

Although no exact solution is available, for this problem the solution appears qualitatively reasonable. The method's ability to handle the complex topological changes on the interface are evident as the bubble deforms during its fall and impacts the film. The structured mesh results are somewhat smoother, and toward the end of the calculation it predicts a more flattened drop than the unstructured mesh. The latter results in a slight increase in its velocity so its final position is not as low. On the whole, the agreement is acceptable. As would be expected the resolution of fine scale features in the interface differs somewhat, but the overall drop velocity and deformation is similar for the two meshes. To capture the fine scale features of the phase interface it would be advantageous to use mesh adaptivity.

Copyright © 2003 John Wiley & Sons, Ltd.

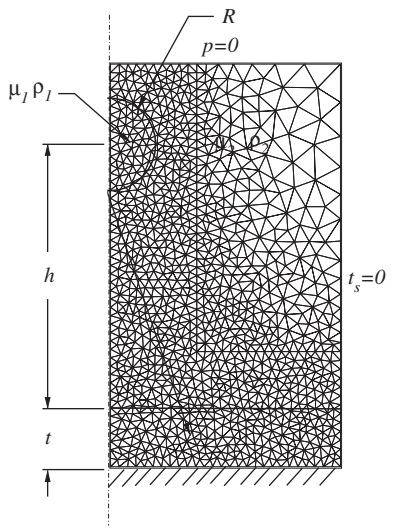


Figure 9. Initial configuration and unstructured mesh for problem of a drop falling under gravity onto a thin film of the same fluid. The solid line indicates the initial position of the drop and thin film interfaces.

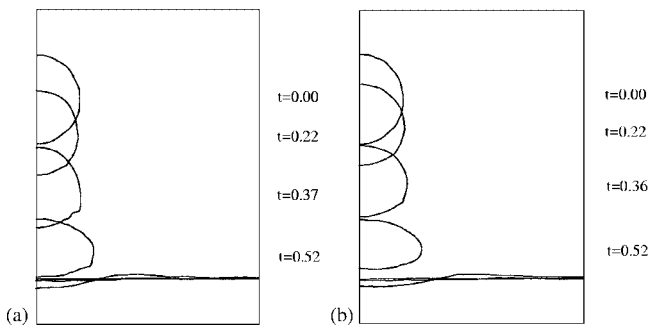


Figure 10. Interface position numerical solution of drop falling onto a thin film at four different time steps both meshes: (a) Mesh 1; and (b) Mesh 2.

9.3. *Terminal velocity of a rising bubble*

In this problem, we consider a bubble which is rising in a fluid of greater density. The computational domain is shown in Figure 13. The following parameters were used in the computation: $d = 1.90$, $\rho = 1.0$, $\mu = 6.0$, $\rho_b = 0.25$, $\mu_b = 1.0$, $g = 20$ and $\sigma = 20.0$. Two dimensionless groups that characterize bubble buoyancy problems are the Eötvös number (buoyancy/capillary), which is defined as

$$E_0 = \frac{g\Delta\rho d^2}{\sigma} \tag{98}$$

Copyright © 2003 John Wiley & Sons, Ltd.

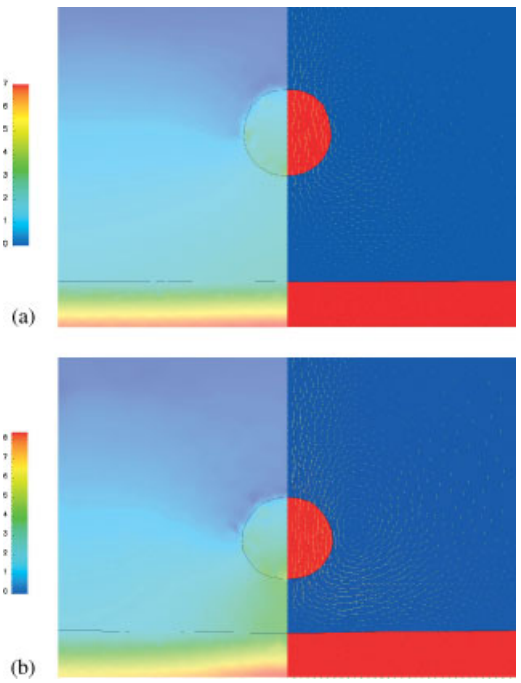


Figure 11. Numerical solution of drop falling on to a thin film at two different time steps. The pressure is plotted along the velocity vectors and the phase interfaces for mesh 1: (a) $t = 0.146$; and (b) $t = 0.292$.

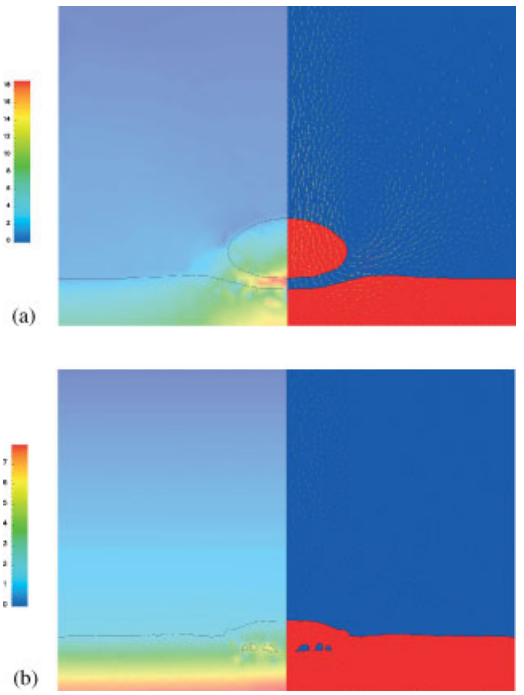


Figure 12. Continuation of results in Figure 11: (a) $t = 0.437$; and (b) $t = 0.583$.

and the Morton number (viscous/capillary)

$$M = \frac{g\mu^4 \Delta\rho d^2}{\rho^2 \sigma^3} \tag{99}$$

where g is the gravitational acceleration, $\Delta\rho$ is the density ratio, d is the diameter of the bubble, σ is the surface tension coefficient and μ is the viscosity of the surrounding fluid. For the above parameters $E_0 = 2.71$ and $M = 2.43$. These parameters were chosen so that the bubble is in the low Reynolds number regime and consequently the bubble should remain roughly spherical throughout the computation.

The bubble and surrounding fluid are initially at rest and subjected to an initial hydrostatic pressure $p = -\rho g z$ where $z = 0$ at the initial position of the free surface. The bubble accelerates due to the buoyancy force and reaches a terminal velocity when the buoyancy force is in equilibrium with the drag force. This classic problem has been studied in detail by several investigators; a thorough review is presented in Reference [22].

Two commonly used terminal velocity approximations are those attributed to Stokes and Hadamard–Rybczynski. From empirical evidence the Stokes approximation is generally valid for small bubbles where recirculation in the bubble is not often observed (Hill's vortex), and

Copyright © 2003 John Wiley & Sons, Ltd.

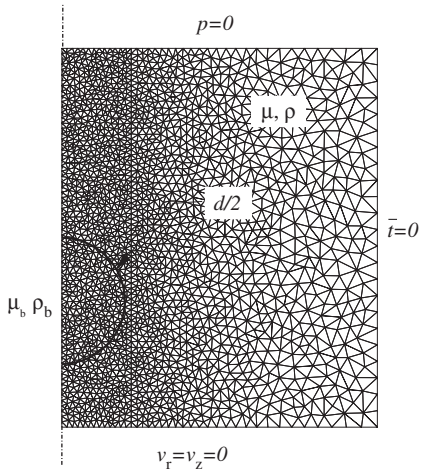


Figure 13. Computational domain for the buoyancy driven bubble.

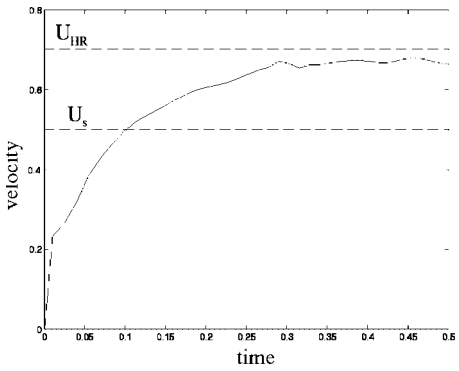


Figure 14. Velocity of the bubble centroid compared to the Stokes (U_S) and Hadamard–Rybczynski (U_{HR}) terminal velocities.

the bubble behaves as if it were a rigid particle. Typically, the Hadamard–Rybczynski approximation, which is valid for larger bubbles where recirculation is observed, serves as an upper bound and the Stokes approximation as a lower bound. Both approximations assume creeping flow ($R_e < 1$) and that the bubble is spherical. The Hadamard–Rybczynski terminal velocity is

$$U_{\mathrm{HR}} = \frac{1}{6}\,\frac{g\,d^2\Delta\rho}{\mu}\left(\frac{2+3\kappa}{1+\kappa}\right) \tag{100}$$

where κ is the ratio of the viscosity of the bubble to the viscosity of the surrounding fluid. The Stokes terminal velocity is

$$U_{\mathrm{S}} = \frac{gd^2\Delta\rho}{18\mu} \tag{101}$$

For the parameters in the computation the predicted Hadamard–Rybczynski and Stokes terminal velocities are $U_{\mathrm{HR}} = 0.702$ and $U_{\mathrm{S}} = 0.501$, respectively.

Figure 14 shows the computed velocity of the bubble centroid along with the Stokes and Hadamard–Rybczynski terminal velocities. The terminal velocity from the computation falls just under the Hadamard–Rybczynski value and above the Stokes value.

9.4. Bubbles rising to a surface

Here we consider the problem of two bubbles of differing diameters but of the same constituent fluid, benzene. The bubbles rise to a free surface in a secondary fluid, water, due to buoyancy. The fluid above the free surface is benzene as well. Figure 15 shows the initial configuration of the bubbles with respect to the surface and the discretization. The larger bubble has a radius of 0.750 cm and the smaller bubble has a radius of 0.375 cm. The two bubbles will

Copyright © 2003 John Wiley & Sons, Ltd.

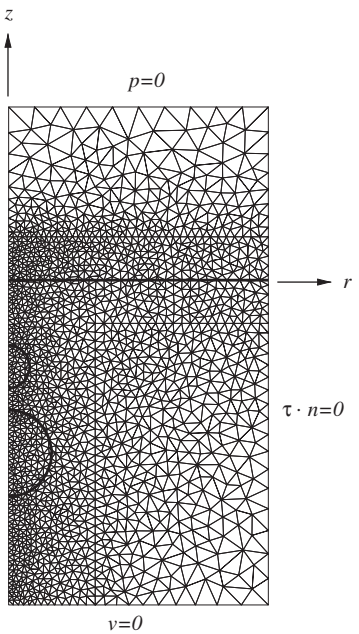


Figure 15. Initial configuration and mesh for problem of two buoyancy driven bubbles. The solid lines indicate the initial positions of the bubbles and the surface.

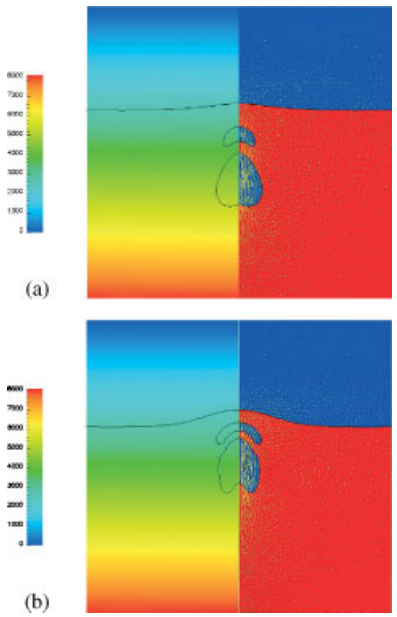


Figure 16. Numerical solution of two bubbles rising to a fluid interface surface at four different time steps for the coarse unstructured grid. The pressure is the plotted on the left-hand side and the velocity vectors and the phase interfaces on the right-hand side (cgs units): (a) $t = 0.146$; and (b) $t = 0.292$.

rise at different rates due to their differing buoyancy forces. The Eötvös numbers for the larger and smaller bubbles are 27.25 and 6.81, respectively; the Morton number, which is independent of the bubble dimension, is 1.77×10^{-9} for both bubbles. The problem is run on a coarse unstructured discretization of three-node triangular elements and fine 80×154 triangular discretization. The unstructured grid is shown in Figure 15; as can be seen, the mesh is refined in the vicinity of the bubbles. The initial conditions for the problem are zero velocity and hydrostatic pressure, and the problem was run for a sufficient period of time so that the merging of the bubbles and their subsequent rising through the free surface can be seen.

Figures 16–19 show the velocity vectors, pressure and interface position for the problem at several time steps during the simulation for both grids.

The results are quite similar until about $t = 0.3$. The only difference is that in the unstructured mesh, a bigger dimple occurs at the bottom centre of the bubble. Later in the run, the results differ more substantially. The top bubble blends with the bottom bubble much earlier in the unstructured mesh simulation. The structured mesh results in fact show a very thin layer of benzene persisting between the benzene above the water and the larger benzene bubble below. It may be that the unstructured mesh provides destabilizing forces that eliminate this

Copyright © 2003 John Wiley & Sons, Ltd.

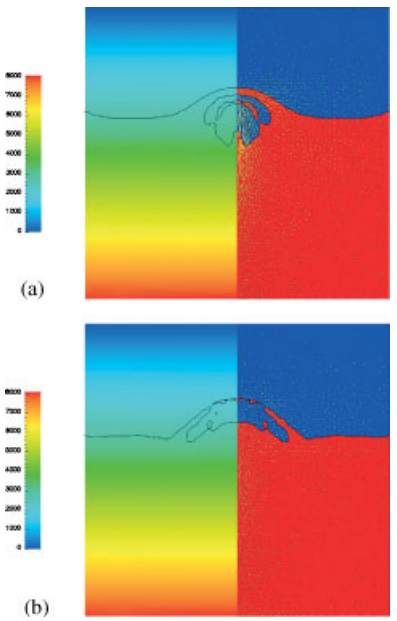


Figure 17. Continuation of results in Figure 16: (a) $t = 0.437$; and (b) $t = 0.583$.

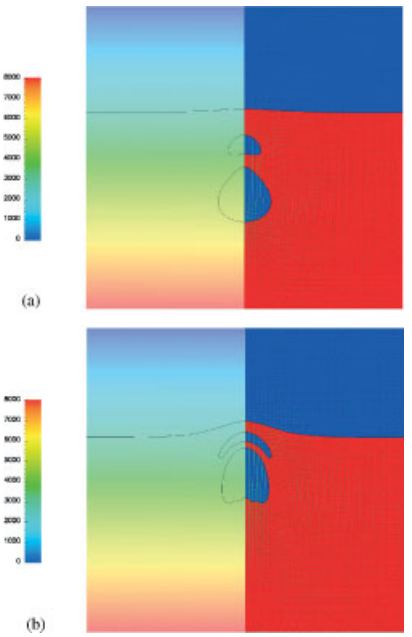


Figure 18. Numerical solution of two bubbles rising to a fluid interface surface at four different time steps for the 80×154 structured grid. The pressure is the plotted on the left-hand side along the velocity vectors and the phase interfaces on the right-hand side (cgs units): (a) $t = 0.146$; and (b) $t = 0.292$.

thin layer. Similar differences also are seen in tracking the breakup of the final benzene into the benzene above the surface. This occurs much faster in the unstructured mesh.

10. CONCLUSIONS

A methodology for treating axisymmetric two-phase flow with surface tension effects by enriched finite elements and level sets has been developed. The velocity field is enriched with the signed distance function so that the velocity gradient discontinuity at the interface within an element is accurately treated. This eliminates the need for a moving mesh or mesh refinement. The method has been primarily developed in the context of linear three-node triangles, but can be extended to higher-order elements.

The position of the fluid interface is tracked via a level set function. This allows for simple construction of the enriched finite elements and also simplifies the computation of the interface curvature.

A modified velocity enrichment function is presented that yields improved accuracy over the standard enrichment function. This modified enrichment function is constructed by solving a Laplace equation for the signed distance function in the blending domain. The resulting signed

Copyright © 2003 John Wiley & Sons, Ltd.

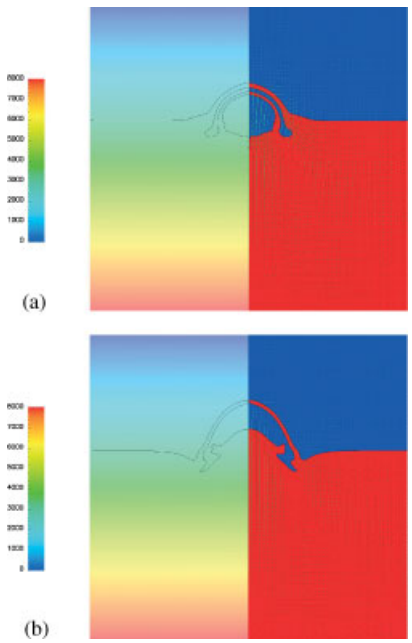


Figure 19. Continuation of results in Figure 18: (a) $t = 0.437$; and (b) $t = 0.583$.

distance function is nearly constant in the blending domain, so that the pathological terms resulting in the blending elements are reduced.

Methods for treating surface tension are developed that allow for the accurate computation of the surface tension force. Both the level set gradient and curvature fields are computed by a least-square projection of the original level set field. This allows for the computation of interface curvature in constant strain elements i.e. three-node triangular elements, whereas direct computation of the level set curvature would yield zero curvature for constant gradient elements. The computational expense of the curvature computations is minimal since the curvature field is only computed where needed (the enriched elements). The surface tension force is then computed by a domain integral instead of a more awkward contour integral. This is facilitated by a polynomial regularization of the Dirac delta function. Since a polynomial approximation to the Dirac function is used standard quadrature can be employed to integrate the surface tension force.

Results show that the enriched method is capable of exactly reproducing a stable two-phase Couette flow (no surface tension) exactly even when the fluid interface occurs in an element. By contrast, methods without enrichment of yield poor results at the interface between the two fluids and the neighbouring elements.

The method is shown to provide a good estimate for the terminal velocity of a bubble rising in a denser fluid as compared to the Hadamard–Rybczynski theory. The method has also been applied to a problem of a free drop falling onto a thin film with the same fluid properties and buoyancy driven bubbles. The method is able to treat complicated topology changes quite effectively. The method is applicable to both structured and unstructured meshes. The agreement between these meshes is generally satisfactory, but in some cases significant

Copyright © 2003 John Wiley & Sons, Ltd.

differences develop. The origin of these differences is not yet understood. However, methods which explicitly track the interface such as ALE would have a difficult time in handling the dramatic topological changes shown in these examples.

ACKNOWLEDGEMENT

The support of the Office of Naval Research is gratefully acknowledged.

REFERENCES

1. Chessa J, Belytschko T. An extended finite element method for two-phase fluids. *Journal of Applied Mechanics* (ASME) 2003; **70**(1):10–17.
2. Belytschko T, Black T. Elastic crack growth in finite elements with minimal remeshing. *International Journal for Numerical Methods in Engineering* 1999; **45**(5):601–620.
3. Moës N, Dolbow J, Belytschko T. A finite element method for crack growth without remeshing. *International Journal for Numerical Methods in Engineering* 1999; **46**:131–150.
4. Belytschko T, Moës N, Usui S, Parimi C. Arbitrary discontinuities in finite elements. *International Journal for Numerical Methods in Engineering* 2001; **50**(4):993–1013.
5. Sukumar N, Chopp DL, Moës N, Belytschko T. Modeling holes and inclusions by level sets in the extended finite element method. *Computer Methods in Applied Mechanics and Engineering* 2000; **190**(46–47): 6183–6200.
6. Wagner GJ, Moës N, Liu WK, Belytschko T. The extended finite element method for rigid particles in Stokes flow. *International Journal for Numerical Methods in Engineering* 2001; **51**(3):293–313.
7. Chessa J, Smolinski P, Belytschko T. The extended finite element method (XFEM) for solidification problems. *International Journal for Numerical Methods in Engineering* 2002; **53**:1959–1977.
8. Renaud M, Dolbow J. Modeling dendritic solidification with the extended finite element method. In *Proceedings of the First MIT Conference on Computational Fluid and Solid Mechanics*, Bathe KJ (ed.). Elsevier: Boston, 2001; 1135–1138.
9. Melenk JM, Babuška I. The partition of unity finite element method: Basic theory and applications. *Computer Methods in Applied Mechanics and Engineering* 1996; **39**:289–314.
10. Chessa J, Wang H, Belytschko T. On the construction of blending elements for local partition of unity enriched finite elements. *International Journal for Numerical Methods in Engineering* 2003; **57**(7):1015–1038.
11. Osher S, Sethian JA. Propagation of fronts with curvature based speed: algorithms based on Hamilton–Jacobi formulations. *Journal of Computational Physics* 1988; **79**:12.
12. Sethian JA. *Level Set Methods and Fast Marching Methods*. Cambridge University Press: Cambridge, MA, 1999.
13. Babuška I, Melenk JM. The partition of unity method. *International Journal for Numerical Methods in Engineering* 1997; **40**:727–758.
14. Belytschko T, Liu WK, Moran B. *Nonlinear Finite Elements for Continua and Structures*. Wiley: New York, 2000.
15. Chorin AJ. Numerical solution of the Navier–Stokes equation. *Mathematics of Computation* 1968; **23**:745–762.
16. Zienkiewicz OC, Codina R. A general algorithm for compressible and incompressible flow, Part I. The split characteristic based scheme. *International Journal for Numerical Methods in Fluids* 1995; **20**:869–885.
17. Zienkiewicz OC, Taylor RL. *The Finite Element Method*, *Volume 3*: *Fluid Dynamics*. Butterworth and Hienemann: Oxford, 2000.
18. Belytschko T, Mullen R. Stability of explicit–implicit mesh partitions in time integration. *International Journal for Numerical Methods in Engineering* 1978; **12**(10):1575–1586.
19. Hughes TJR, Liu WK. Implicit-explicit finite-elements in transient analysis—implementation and numerical examples. *Journal of Applied Mechanics* (ASME) 1978; **45**(2):375–378.
20. Belytschko T, Daniel WJT, Ventura G. A monolithic smoothing-gap algorithm for contact-impact based on the signed distance function. *International Journal for Numerical Methods in Engineering* 2002; **55**(1):101–125.
21. Belytschko T, Lu YY, Gu L. Element-free Galerkin methods. *International Journal for Numerical Methods in Engineering* 1994; **37**:229–256.
22. Clift R, Grace JR, Weber ME. *Bubbles, Drops and Particles*. Academic Press: New York, 1978.

Copyright © 2003 John Wiley & Sons, Ltd.